# Modification of halloysite lumen with dopamine derivatives as filler for antibiofilm coating

Marina Massaro [a,1], Maria Laura Alfieri [b,1], Giorgio Rizzo [c], Francesco Babudri [c], Raquel Barbosa de Melo [d], Teresa Faddetta [a], Giuseppe Gallo [a], Alessandra Napolitano [b], Rita Sanchèz-Espejo [d], César Viseras Iborra [d,e], Serena Riela [a,*]

[a] *Dipartimento di Scienze e Tecnologie Biologiche, Chimiche e Farmaceutiche (STEBICEF), University of Palermo, Viale delle Scienze, 90128 Palermo, Italy*

[b] *Dipartimento di Scienze Chimiche, Universita` di Napoli Federico II, Via Cinthia 4, 80126 Napoli I, Italy*

[c] *Dipartimento di Chimica, Universita` degli Studi di Bari "Aldo Moro", Via Edoardo Orabona 4, 70126 Bari, Italy*

[d] *Department of Pharmacy and Pharmaceutical Technology, Faculty of Pharmacy, Campus of Cartuja, University of Granada, 18071 s/n, Granada, Spain*

[e] *Andalusian Institute of Earth Sciences, CSIC-UGR. Avenida de las Palmeras 4, 18100 Armilla, Granada, Spain*

A B S T R A C T:

*Hypothesis:* Development of nanocomposite coating with antibiofilm properties is of fundamental importance to efficient fight biofilm formation preventing infections in biomedical area. In this context, halloysite nanotubes (HNTs), biocompatible and low-cost clay mineral, have been efficiently used as filler for different polymeric matrices affording several nanocomposites with appealing antimicrobial properties. The modification of HNTs surfaces represents a valuable strategy to improve the utilization of the clay for biological purposes.

*Experiments.*Herein, the covalent modification of the HNTs lumen with properly designed dopamine derivatives with different perfluoroalkyl chain length is reported. The obtained nanomaterials are thoroughly characterized by several techniques. As proof of concept the antibiofilm properties on *E. coli* strain of the nanomaterials are assayed as well. Finally, the HNTs fillers were introduced into a polydopamine matrix allowing for the preparation of functional coatings, resistant to formation of microbial biofilms.*Findings:* All characterization methods proved the selectivity of the modification and the increased hydropho-bicity of the lumen. In particular $^{27}$Al solid state nuclear magnetic resonance (NMR)

spectra showed a upfield shift of the Al signal. Studies on the antibiofilm properties highlighted different activities according to the length of perfluoroalkyl chains of organic molecules as proved by $^{19}F$ solid state NMR spectra. The synthetized materials were promising for future application as coatings on medical implants.

*Keywords:* Halloysite nanotubes Lumen modification Dopamine derivatives Antibiofilm formation Coating

## 1. Introduction

Bacteria produce biofilms as part of their survival strategies [1]. Although they are important in symbiotic functions and biogeochemical cycles [2], biofilms are dangerous to humans and cause more than 80% of chronic microbial infections, causing a variety of problems in the environment, food industry, and medical implants and devices [3]. In 2019, C´amara et al. presented the global financial impact of biofilms, estimated to represent almost US$ 4,000 billion per year, with two-thirds due to corrosion and the remainder composed of a mix of sec-tors, with a relatively large part falling on human health, in particular the formation of biofilms on wounds [4].

In this context, *Escherichia coli*, a Gram-negative bacterium, is one of the major causes of infection that forms biofilms on the surfaces of materials used in the above-mentioned sectors [5].

In the last years, several approaches to fight biofilms formation, based on the surface modification with an antimicrobial coating, have been carried out [5,6]. The coating involves, for example, the use of active agents (e.g. antibiotics, metal nanoparticles, etc.), light-activated molecules (e.g. photosensitizers such as $TiO_2$ or perfluoroalkyl phtha-locyanine) [6,7], or the introduction of organic/inorganic fillers (carbon nanotubes, silica, clay minerals, etc.) [8–12] that improves both the mechanical properties of the coating and its interfacial interaction with the active agents.

In particular, clay minerals, layered phyllosilicates, such as lamellar montmorillonite (MMT) that consists in an octahedral layer intercalated between two tetrahedral layers (2:1), were used as a coating to enhance the antibacterial properties of Mg alloy AZ31 in the presence of genta-micin; indeed, the positively charged MMT surface can interact with the negatively charged membrane of the bacteria, by electrostatic forces, thus assisting gentamicin in its bactericidal and bacteriostatic action.[13].

Among 1:1 clay minerals, halloysite, due to its tubular structure with an empty lumen (HNTs) has been efficiently used as filler for the development of antibacterial nanomaterials since it can improve both the mechanical properties of the coatings and can further load active substances into the lumen [14]. For example, gentamicin/HNTs nano-material was reported by Lvov *et al.* as filler for poly-(methyl methac-rylate), which has long been used as bone cement [15]. Similarly, HNTs@ZnO nanomaterial was used as filler for polyethylene and poly-vinyl chloride to develop antibacterial nanocomposite for urinal cathe-ters [16].

Covalent modifications of HNTs surfaces offer the possibility to obtain fillers with tunable properties

[17–19]. In this context, several studies reported the covalent modification of the HNTs external surface by grafting suitable organosilanes for the development of nanomaterials with hierarchical structures for applications in several fields [20]. In addition, the loading or the grafting of active species with antimicrobial action led to the synthesis of nanosystems used for example as anti-bacterial for wound healing, and active food packaging to mention only a few [21–25].

Up to now, only few examples are reported in literature about the modification of HNTs inner surface, and they are based on the linkage between the aluminol groups and organophosphorus compounds [26], phenylboronic acids [27] and catechol-based molecules [28].

Recently, it was shown that a key role to enhance the antibacterial performance of the nanocomposites is played by their hydrophobicity [29]. For example, fluoropolymers, known for their high hydrophobicity [30], were used to develop nanocomposites with antifouling properties against microbes, foulants, and blood, and possessing also outstanding self-cleaning activity [31].

Based on this premise, herein, we report the covalent modification of by ad hoc synthesized perfluorinated hydrophobic mole-cules namely N-perfluoroacyl dopamides, as fillers for the development of antibiofilm coatings. The catechol moiety of the *N*-perfluoroacyl molecules ensures the selective binding to the HNTs lumen [32], whereas the perfluoroalkyl chains could add antibiofilm and hydro-phobic properties to HNTs filler (Fig. 1).

The obtained fillers were characterized through thermogravimetric analysis, FT-IR spectroscopy, dynamic light scattering and ς-potential measurements. The selective binding of the organic molecules with HNTs lumen was verified by $^{27}$Al solid state NMR spectroscopy. The morphology was studied by high angle annular dark field transmission electron microscopy (HAADF/STEM) coupled with Energy Dispersive X-ray spectroscopy (EDX). The increased hydrophobicity of the HNTs lumen after *N*-perfluoroacyl dopamides binding was highlighted by spectrofluorometric measurements using pyrene as a probe.

As proof of concept, the antibiofilm formation properties of the ob-tained fillers on *E. coli* were investigated by *in vitro* assay, HAADF/STEM investigations and $^{19}$F solid state NMR spectroscopy. To explain the biological results, contact angle measurements were also performed. Finally, the most promising nanomaterials were used as fillers for pol-ydopamine matrix chosen as a model of coating because of its well-known biocompatibility and universal substrate-independent coating properties [33].

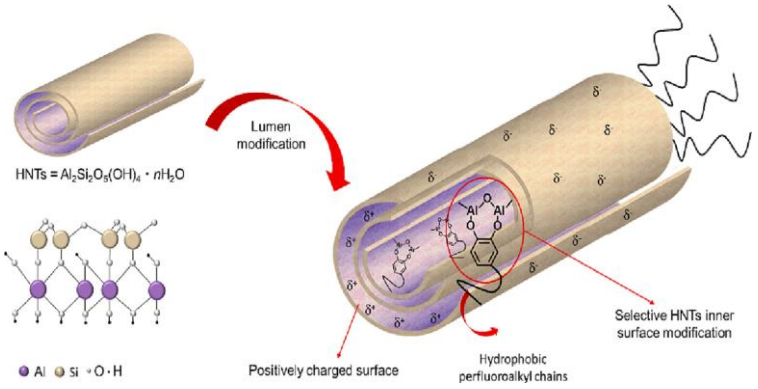


**Scheme 1.** Synthesis of *N*-perfluoroacyl dopamide molecules **1**–**6**.

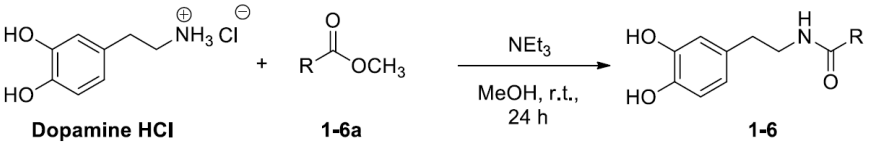


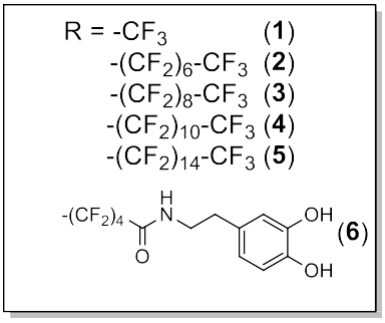


**Fig. 1.** Schematic representation of the HNTs based filler synthesized.

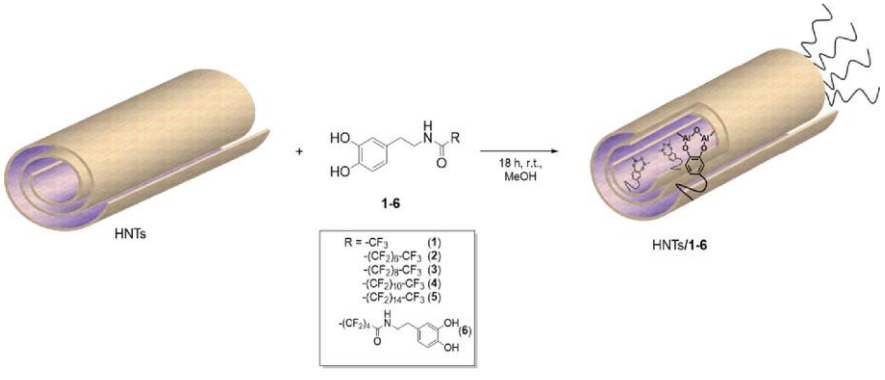


**Scheme 2.** Schematic representation of the synthesis of HNTs/**1**–**6** nanomaterials.

## 2. Results and discussion

Halloysite is a multilayer nanotube that possesses an empty lumen with suitable dimension to host molecules. To selectively modify the HNTs lumen, *N*-perfluoroacyl dopamide molecules (**1**–**6**) were synthesized following the experimental procedure, reported for the *N*-tri-fluoroacetyl dopamide [34], depicted in Scheme 1, by reacting dopamine hydrochloride with the perfluoroacyl methyl ester (**1-6a**) affording final molecules with satisfactory yields greater than 90% except for **5** (26%) possibly due to the poor solubility of the corre-sponding perfluorinated ester in the reaction medium. Dopamine de-rivatives were chosen because of the high affinity of the catechol moieties towards the aluminol groups in HNTs lumen. In this way, a coordination bond between the catechol and the alumina rich-surface with a 1:1 bidentate complexation in the final HNTs/**1**–**6** nano-material was expected to occur as reported [32].

Inspired by the pioneering works of Lvov, Takahara *et al.* [26,28] the loading of **1**–**6** compounds into halloysite was carried out by mixing an aqueous dispersion of halloysite (5 mL) with a concentrated **1**–**6** solution in MeOH ($10^{-2}$ M, 1 mL) (Scheme 2). Then, the obtained suspension was stirred and maintained under vacuum for 3 to 5 min, resulting in light fizzling, which indicated that air was released from the tubes.

Once the vacuum was removed, the solution entered the lumen and the loaded compound adsorbed within the tubes. This procedure was repeated 2 to 3 times to improve the loading efficiency.

After the work-up, the amounts of compounds loaded into HNTs were determined by TGA. Results in Table 1 indicate that in almost all cases a loading ranging from 2 to 5 wt% was observed following the molecular weight of the compounds. A slight decrease in the loading was observed in the case of HNTs/**5** and HNTs/**6** nanomaterials and this could likely be explained by some steric hindrance phenomena. No loading was instead observed in the case of HNTs/**1** nanomaterial probably because of the higher aqueous solubility of compound **1** compared to the other *N*-perfluoroacyl dopamides, and therefore, given the conditions of the loading procedure, it can be expected that it ex-hibits a lower or null affinity for HNTs lumen.

Thermoanalytical curves of HNTs/**4** and HNTs/**6** (see Fig. S1 for the others) are reported in Fig. 2a, where that of pristine HNTs is reported as well for comparison. All curves showed the typical weight losses of halloysite in the range 100–150 °C and 450–550 °C due to the removal of physically adsorbed and interlayer water molecules of the clay [35]. The TG curves of HNTs/**4** and HNTs/**6** also showed an additional weight loss in the range 250–400 °C attributable to the degradation and vola-tilization of organic moieties. From the residual matter at 900 °C it was possible to calculate the loading of the different compounds reported in Table 1.

In Fig. 2b the FT-IR spectra of HNTs/**4** and HNTs/**6** nanomaterials, chosen as models, and that of pristine HNTs for comparison (see SI for other spectra) are reported. As known [36], the FT-IR spectrum of pristine HNTs shows some typical vibration bands at ca. 3622 $cm^{-1}$ attributable to O–H stretching vibrations of the

inner surface hydroxyl groups, and the bands at 3484 and 1645 $cm^{-1}$ due to the O–H stretching and bending vibrations, respectively, of adsorbed water. Furthermore, several bands are present in the range 1100–400 $cm^{-1}$ attributable to the vibration motions of Si-O-Si groups. After modification, in the FT-IR spectra of the nanomaterials new bands are present. In particular, the bands at ca. 1690 $cm^{-1}$, attributable to the C–O stretching of the amide groups, and the bands in the range 1550 – 1420 $cm^{-1}$ due to C–C, C–N stretching are observed. All these findings further confirm the successful loading of the *N*-perfluoroacyl dopamides into HNTs.

Dynamic light scattering experiments were performed in an aqueous dispersion to characterize the diffusion dynamics of HNTs/**4** nano-material, chosen as model. It was assumed that since the interaction of perfluoacyl dopamides occurs with HNTs lumen, no differences in the aqueous diffusion of nanomaterials were observed by varying the number of alkyl chains. HNTs are anisotropic objects with a high aspect ratio, which can change with functionalization. Moreover, the particle's ability to interact and aggregate can also depend on surface modifica-tion. Thus, a detailed quantitative analysis of the results was hampered. Valuable information was achieved by using the Stokes-Einstein equa-tion to calculate the average diameter of the equivalent sphere, which can be considered as an index to follow the changes in particle di-mensions and interparticle aggregation. A single translational diffusion mode was observed in all cases investigated with Z-average sizes (i.e., the intensity weighted mean diameters) (Table S1) similar to those of pristine HNTs. These findings confirmed the selective interaction of the *N*-perfluoroacyl dopamides with HNTs lumen.

In line with DLS, Z-potential measurements highlighted a slight in-crease in the ς-potential value of the nanomaterial (Table S1) in comparison to that of pristine HNTs (-19 mV), in accord with halloysite modifications [37].

To further confirm the confinement of the molecules inside HNTs lumen solid state $^{27}Al$ NMR spectroscopic studies were performed (Fig. 3). The $^{27}Al$ NMR spectrum of HNTs showed the typical peak at ca. 7.16 ppm arising from the resonance of the aluminium atoms octahedral coordinated at the inner halloysite surface [38]. As reported elsewhere, indeed, by $^{27}Al$ MAS-NMR it is not possible differentiate between octa-hedral Al atoms both in the lumen and on interlayer sites since an overlap of the signals occurs [39]. After the coordination of the catechol-based molecules, this peak was upfield shifted from 7.16 ppm to 6.68 ppm, as shown by the solid state $^{27}Al$ NMR spectrum of HNTs/**2** nano-material, chosen as an example (see SI for other spectra). This finding, led us to hypothesize that some Al atoms (the ones in the lumen) possess a chemical environment of different from that of pristine HNTs; sug-gesting the selective interaction of perfluoroacyl dopamides with the lumen, as already reported for other systems [40].

**Table 1.** Loading (wt%) of the **1**–**6** molecules into HNTs lumen.

| Entry | Molecule 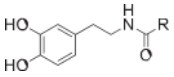 | HNTs based Nanomaterial | Loading / wt%[(a)] | Degree of functionalization / mmol $g^{-1}$ |
|---|---|---|---|---|
| 1 | R = $–CF_3$ | HNTs/**1** | / | / |
| 2 | R = $–(CF_2)_6–CF_3$ | HNTs/**2** | 3.0 | 0.06 |
| 3 | R = $–(CF_2)_8–CF_3$ | HNTs/**3** | 4.0 | 0.06 |
| 4 | R = $–(CF_2)_{10}–CF_3$ | HNTs/**4** | 5.2 | 0.07 |
| 5 | R = $–(CF_2)_{14}–CF_3$ | HNTs/**5** | 3.0 | 0.03 |
| 6 | 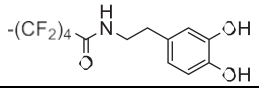 | HNTs/**6** | 2.1 | 0.04 |

[a]Estimated by TGA.

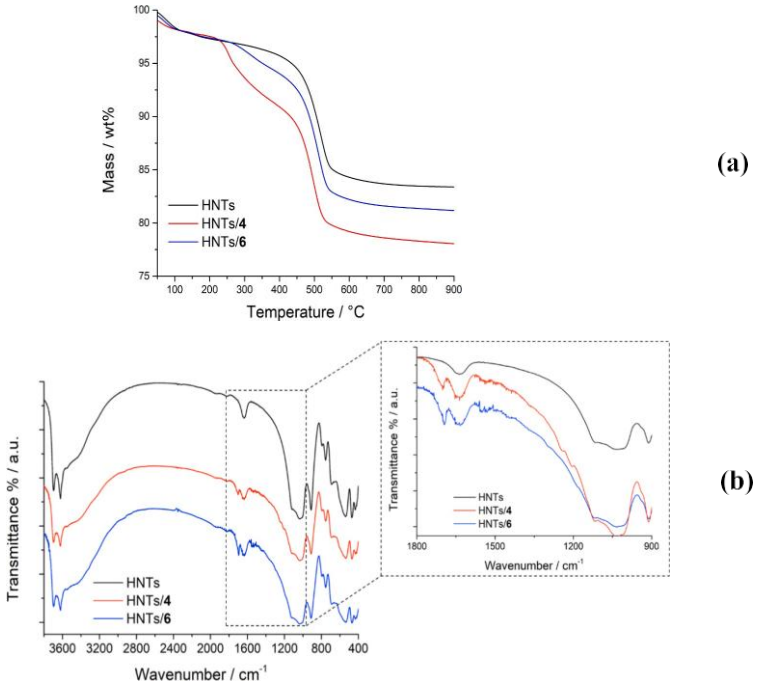


**Fig. 2.** (a) Thermoanalytical curves and (b) FT-IR spectra of HNTs, HNTs/**4** and HNTs/**6** nanomaterials.

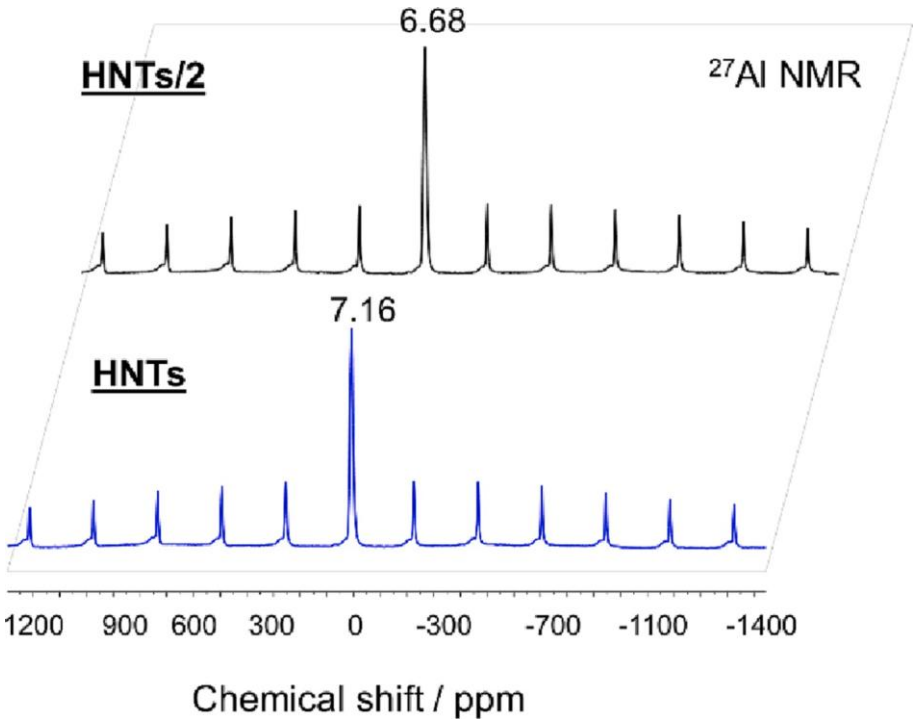


**Fig. 3.** $^{27}$Al solid state NMR spectra of HNTs and HNTs/**2** nanomaterial.

The morphology of the nanomaterials was imaged by TEM and high-angle annular dark field scanning transmission electron microscopy (HAADF-STEM). In Fig. 4 is reported the TEM image of the HNTs/**4** nanomaterial, once again chosen as the nanomaterials model. As it is possible to observe, the characteristic tubular structure of the halloysite was preserved after the loading (Fig. 4A).

Energy-dispersive X-ray spectroscopy (EDS) elemental mapping showed that compound **4** was present on the overall surface of the tubes, as highlighted by the distribution of F atoms (highlighted in orange in all samples) (Fig. 4B-C). Moreover, close observation of the tubes showed the presence of F atoms mainly localized in the proximity to the HNTs lumen (Fig. 4D). EDX spectrum on a selected area showed the presence of the Al and Si related to halloysite with the presence of C and F atoms of the organic molecule loaded. Furthermore, statistical analysis of the mean inner diameter of HNTs/**4** nanomaterial showed a slight decrease in the diameter in comparison to pristine HNTs (from 14.9 nm to ca. 11 ± 3 nm) further confirming the inner surface modification.

Fluorescent probes have been successfully used for decades to study biological and chemical environments, therefore, to confirm the in-crease of hydrophobicity of the HNTs lumen after the linkage of *N*-perfluoroacyl dopamide, the interaction of selected nanomaterials (HNTs/**2** and HNTs/**5** nanomaterials with 7 and 15 carbon atoms in the perfluoroalkyl chains, respectively) with pyrene was studied by fluo-rescent titration.

In Fig. 5 the trend of the variation of the emission intensity of pyrene as a function of the amount HNTs/**2** and HNTs/**5** nanomaterials (up to 0.3 mg $mL^{-1}$) the emission of pyrene increases (with the highest values observed in the case of HNTs/**5** nanomateria  given its higher number of carbon atoms) thus confirming a hydrophobic interaction with HNTs based nanomaterials. It is noteworthy that in the same experimental conditions, no change in the emission intensity of pyrene was observed in the presence of pristine HNTs. All these findings confirm the increased hydrophobicity of HNTs because of the presence of the *N*-perfluoroacyl dopamide molecules [41].

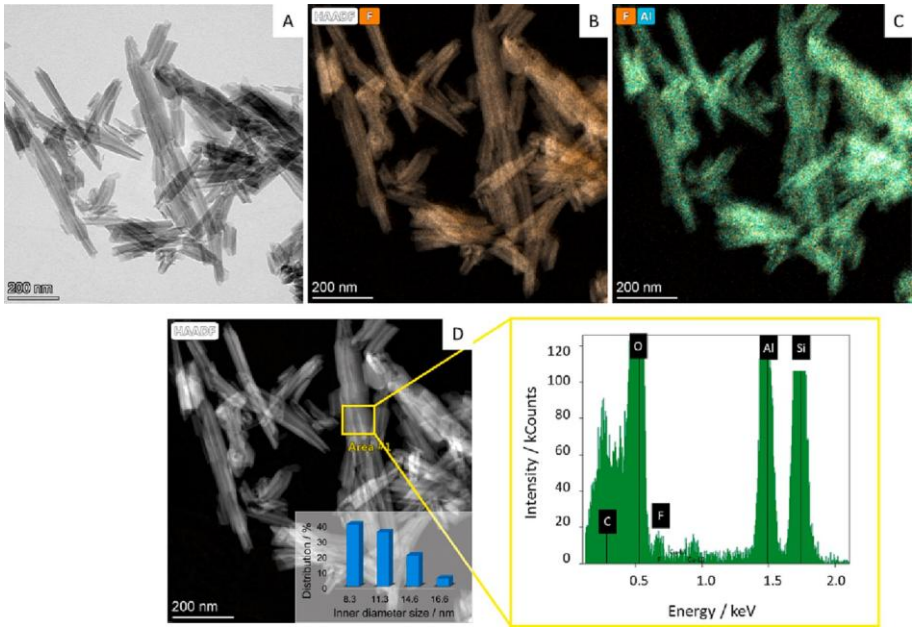


**Fig. 4.** (A) TEM image of the HNTs/**4** nanomaterial, (B-C) EDX elemental mapping images. (D) EDS analysis on the selected area. The inset shows the HNTs/**4** diameter size distribution (number of counts = 25).

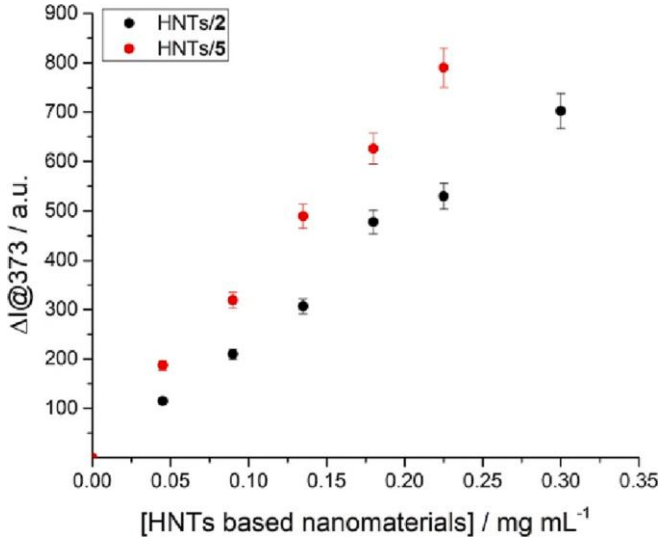


**Fig. 5.** Trend of the variation in pyrene emission at 373 nm as a function of HNTs/**2** and HNTs/**5** concentration (0 –0.3 mg $mL^{-1}$) in water, at 25 °C; [pyrene] = $2 \times 10^{-7}$ M. Reported are the mean ± standard deviation values of two independent experiments.

### 2.1. *Evaluation of the antimicrobial and antibiofilm formation properties*

Firstly, to evaluate any antimicrobial activity of compounds **2**–**6**, they were assayed *in vitro* against planktonic forms of *E. coli* bacterial tester. This analysis revealed that the molecules did not exert inhibition of bacterial growth in the respect to control growth conditions. Similar results were obtained by treating the bacterial tester with the HNTs/**2**–**6** nanomaterials; also in this case, indeed, no inhibition of the planktonic growth of bacterial testers was observed.

However, analysis of the biofilm formation, revealed that all HNTs based nanomaterials showed a strain specific inhibition (Fig. 6). In particular, HNTs/**2** and HNTs/**3** nanomaterials nanomaterials caused a significant reduction ($p < 0.05$) of *E. coli* biofilm formation with respect to untreated culture (control), with HNTs/**3** showing the highest inhibition (42%). This result is particularly interesting since pristine HNTs revealed, on the contrary, a significant ($p < 0.05$) increment (22%) of biofilm formation with respect to untreated culture [42]. On the con-trary, no biofilm inhibition was observed in the presence of **2**–**6** given its higher number of carbon atoms) thus confirming a hydrophobic interaction with HNTs based nanomaterials. It is noteworthy that in the same experimental conditions, no change in the emission intensity of pyrene was observed in the presence of pristine HNTs. All these findings confirm the increased hydrophobicity of HNTs because of the presence of the *N*-perfluoroacyl dopamide molecules [41].

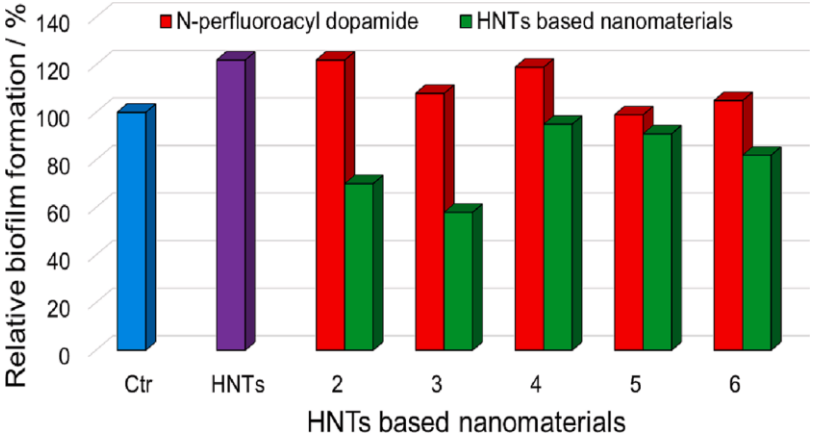


**Fig. 6.** *E. coli* biofilm formation in the presence of **2**–**6** molecules and HNTs based nanomaterials. Inhibition values are reported with respect to biofilm of untreated cultivations used as control condition. $p < 0.05$ according to ANOVA test.

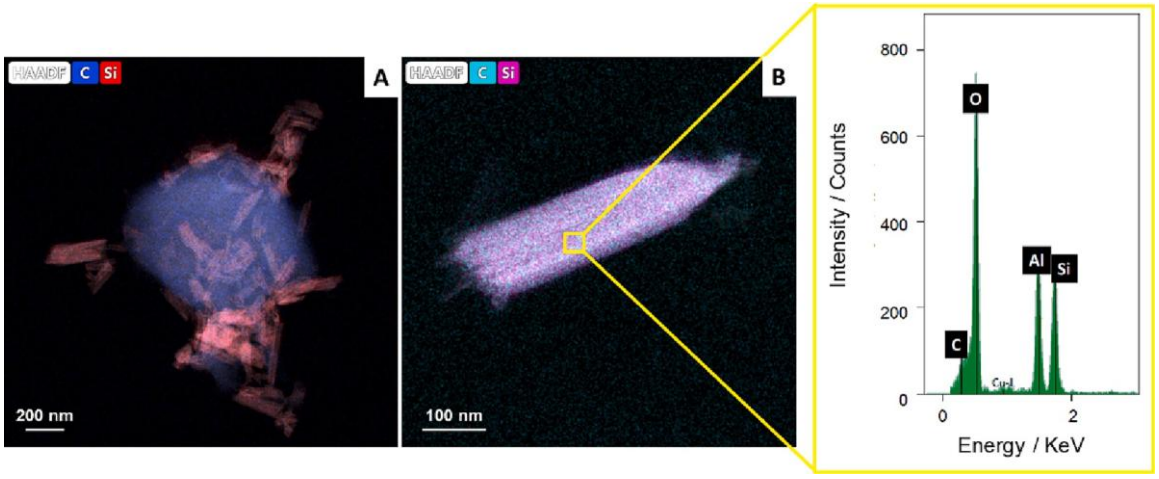


**Fig. 7.** TEM images of a representative area of *E. coli* biofilm treated with (A) HNTs/**5** and (B) HNTs/**2** nanomaterials. The inset shows the EDX analysis of the selected area.

### 2.2. *Evaluation of the antimicrobial and antibiofilm formation properties*

Firstly, to evaluate any antimicrobial activity of compounds **2**–**6**, they were assayed *in vitro* against planktonic forms of *E. coli* bacterial tester. This analysis revealed that the molecules did not exert inhibition of bacterial growth in the respect to control growth conditions. Similar results were obtained by treating the bacterial tester with the HNTs/**2**–**6** nanomaterials; also in this case, indeed, no inhibition of the planktonic growth of bacterial testers was observed.

However, analysis of the biofilm formation, revealed that all HNTs based nanomaterials showed a strain specific inhibition (Fig. 6). In particular, HNTs/**2** and HNTs/**3** nanomaterials nanomaterials caused a significant reduction ($p < 0.05$) of *E. coli* biofilm formation with respect to untreated culture (control), with HNTs/**3** showing the highest inhibition (42%). This result is particularly interesting since pristine HNTs revealed, on the contrary, a significant ($p < 0.05$) increment (22%) of biofilm formation with respect to untreated culture [42]. On the con-trary, no biofilm inhibition was observed in the presence of **2**–**6** molecules. The latter result is important since it highlights the impor-tance to use HNTs to enhance the bioavailability of the molecules, therefore, increasing their biological activity.

The inhibition of biofilm formation by HNTs/**2** nanomaterial was further analyzed by HAADF/STEM investigations. Fig. 7 shows a portion of the *E. coli* biofilm treated with HNTs/**2** and HNTs/**5** nanomaterials. As it is possible to observe in Fig. 7A, in the case of HNTs/**5** nanomaterial, which has shown poor activity (92% inhibition of biofilm formation), the nanomaterial still maintains the tubular morphology as observed in Fig. 4. In addition, the nanomaterial is embedded in a carbon-containing matter likely to be due to the *E. coli* cell biofilm, as inferred from the chemical elemental map extrapolated from EDX measurements. This result is in

agreement with that already reported about the interaction of HNTs with bacterial biofilms [42].

Conversely, in the HNTs/**2** treated *E. coli* biofilm image (Fig. 7B), the formation of biofilm was inhibited (by 70%) by the action of the nanomaterial, and the *E. coli* cells probably were in their planktonic form and unable to embed the HNTs/**2** nanomaterial, as it has been inferred from the EDX analysis and the elemental map extrapolated from it, in agreement with the observations reported for other kinds of modified HNTs nanomaterials [43].

The different antibiofilm activities among the different nano-materials could be explained considering the interaction of **2**–**6** mole-cules with HNTs lumen. It was hypothesized that molecules with shorter fluoroalkyl chains could be more available for interaction with bacteria.

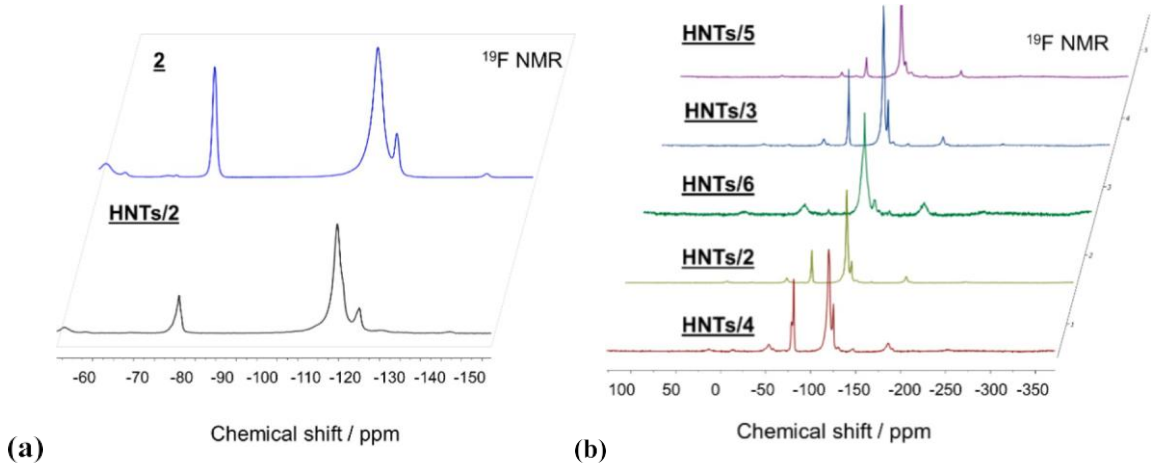


**Fig. 8.** $^{19}$F solid state NMR spectra of (a) **2** and HNTs/**2** nanomaterial; (b) HNTs/**2**–**6** nanomaterials.

**Table 2.**Contact angle values for HNTs, HNTs/**2** and HNTs/ **6** nanomaterials.

| **Sample** | θ / ° |
|---|---|
| HNTs | 30.7 ± 1.5 [46] |
| HNTs/**2** | 45.7 ± 2.3 |
| HNTs/**6** | 29.3 ± 1.9 |

Due to their chemical composition, HNTs possess negatively charged external surface, positively charged lumen and interlayers in a wide pH range. Thus, *E. coli* cells, negatively charged [44,45], could be attracted to the positively charged HNT interlayers, interacting with **2** and **3** molecules, which could exert their antibiofilm activity [7]. On the contrary, longer fluoroalkyl chains, as in **4** and **5** molecules, could interact with each other by hydrophobic interactions, folding them-selves inside lumen, therefore they are not available for the interaction with bacteria. Similarly, **6** molecules, possessing two catechol heads, are totally confined

inside HNTs lumen.

To support these hypotheses, $^{19}F$ solid state NMR spectra of the HNTs/**2**–**6** nanomaterials were recorded. In Fig. 8a, the $^{19}F$ NMR spectra of **2** and HNTs/**2** nanomaterial are reported. The $^{19}F$ solid state NMR spectrum of **2** showed the typical resonance peaks attributed to the fluorine atoms in the perfluoroalkyl chain. In particular, the peak at ca. -79.53 ppm related to the $-CF_3$ groups, and the signals in the range -119 - -123 ppm due to the resonance of the $-CF_2$ groups were observed. After the coordination with HNTs, the peaks are slightly affected by the presence of HNTs, further indicating that the interaction occurs mainly with the catechol moieties.

Similar results were obtained in the case of all the nanomaterials obtained. However, as it is possible to observe in Fig. 8b, the peak related to $-CF_2$ groups at ca. -123 ppm in the case of HNTs/**5** nano-material is less resolved, indicating a change in the chemical environment of **5**, probably due to hydrophobic interactions between the chains in the confined HNTs lumen. To further confirm our hypotheses, contact angle (θ) measurements on HNTs/**2** and HNTs/**6** nanomaterials, chosen as model, were per-formed and the obtained results are listed in Table 2.

θ values of a drop of water onto a solid support, indeed, are related to the hydrophobicity of the surface. As it is possible to note from Table 2, the HNTs/**6** nanomaterial shows a θ value close to that of pristine HNTs [46], indicating that the hydrophobicity of the surface is not altered after modification in agreement with the **6** confinement in HNT lumen. Conversely, an increase in the θ value in comparison to that of pristine HNTs was observed in the case of HNTs/**2** nanomaterial. The increase of θ value is consistent with the hydrophobic nature of the perfluoroacyl dopamide molecules loaded into the HNT lumen and the extension of their fluorine tails at the edges of nanotubes as above hypothesized. These findings further explain the antibiofilm properties of HNTs/**2** nanomaterial.

Encouraged by these results, to develop innovative coating materials as antibiofilm agents, HNTs/**2** nanomaterial was used as a filler for polydopamine (PDA), a choice dictated by the well known ability of this system to form a strongly adhesive film on solid surfaces.

To achieve this goal, the classical polymerization procedure of dopamine under alkaline conditions in air was discarded, and the oxidation was preferably run in a slightly acid medium using $NaIO_4$ as an oxidizing agent to better control film thickness. The reaction was run on dopamine at 10 mM in the presence of HNTs based filler with glass substrates dipped into the reaction mixtures. Recently, some of us found that using this methodology, the resulting nanocomposite film shows HNTs present on the glass surface, and this could be beneficial for future applications [47]. It was indeed found that in acidic media, being the tubes in their zwitterionic form (pI ca. 6.5), they tend to aggregate each other, minimizing the interaction with the growing PDA polymer, and this causes that HNT fillers are mainly present at the surface of the PDA coating.

The so-obtained coatings were tested for their antibiofilm properties and analyzed by HAADF/STEM investigations. In Fig. 9, the images relative to a representative area of *E. coli* biofilm as a control (Fig. 9A),

the *E. coli* biofilm in the presence of the PDA coating (Fig. 9B), and in the presence of the nanocomposite coating PDA-HNTs/**2** (Fig. 9C) are re-ported. As it is possible to infer from the carbon atoms elemental mapping extrapolated by EDX measurements (yellow spots in Fig. 9A and B), the bacterial biofilm showed ellipsoidal and lobed shaped cells. Conversely, after treatment with the nanocomposite coating PDA-HNTs/ **2**, a different morphology was observed (Fig. 9C). In this case, the ellipsoidal and lobed shape of bacterial biofilm cells is not observable, probably due to the inhibition of biofilm formation exerted by the nanocomposite coating. In particular, Fig. 9C shows the presence of HNTs randomly dispersed on its surface (as highlighted by the blue spots referred to Al atoms and red arrows in Fig. 9C).

## 3. Conclusion

Nowadays, biofilm formation represents one of the major problems related to healthcare and thus, finding effective solutions for its inhi-bition is a great challenge. Thus, development of nanocomposite coating with antibiofilm properties is of fundamental importance to efficient fight biofilm formation preventing infections in biomedical area. Herein we reported the synthesis and characterization of HNTs based fillers for the development of nanocomposite coatings with antibiofilm properties. To reach this objective, HNTs lumen was modified with properly synthetized molecules bearing a catechol moiety, able to selective coordinate the aluminol rich inner HNTs surface, and perfluoroalkyl chains which increased the hydrophobicity of the lumen. The successful synthesis of the different nanomaterials was confirmed by TG analysis and FT-IR spectroscopy, whereas the selective HNTs lumen modification was proved by DLS and ς-potential measurements and by solid state $^{27}$Al NMR spectra. In the latter experiment upfield shift of the typical resonance peak of aluminium, further confirmed the interaction with the perfluoroacyl dopamides. HAADF/ STEM investigations showed that the morphology of HNTs was pre-served and that the organic molecules are well dispersed inside the tubes as shown by the elemental maps extrapolated by EDX measurements and statistical analysis of the lumen mean dimensions.

As proof of concept of the feasibility of use of the nanomaterials synthetized for biological applications, their biofilm inhibition growth properties were tested on *E. coli* strain by *in vitro* assays and by HAADF/ STEM investigations. It was shown that among the different molecules used, the ones with better antibiofilm performances were those with shorter perfluoroalkyl chains as a consequence of a good balance be-tween the hydrophobic character and the coordination inside the lumen determining their availability and efficient interaction with the bacteria as proved also by solid state $^{19}$F NMR studies.

Finally, the most promising nanomaterials were used as filler of a polydopamine matrix, chosen as a paradigm for implementation of bioactive coatings. The obtained nanocomposite coatings were suc-cessfully assayed for *E. coli* biofilm formation inhibition as highlighted by HAADF/STEM investigations.

In comparison to other reported works [13,48], the results presented highlight the importance to exploit halloysite nanotubes, a natural available, biocompatible and low-cost nanomaterial, for the develop-ment of

nanocomposite coatings with antibiofilm formation properties for implementation of biomedical devices and other related applica-tions. In addition, the chemical composition of halloysite external sur-face allows for its selective functionalization too increase interfacial properties of the clay, to be dispersed in other polymeric matrices that could be useful for biological applications [49].

The work herein reported puts a step forward to the design of novel halloysite nanomaterials for the industrial scale-up of the synthesis of antimicrobial coatings for application in several fields, especially in the biomedical one as example in the coating of implants or in tissue regeneration.

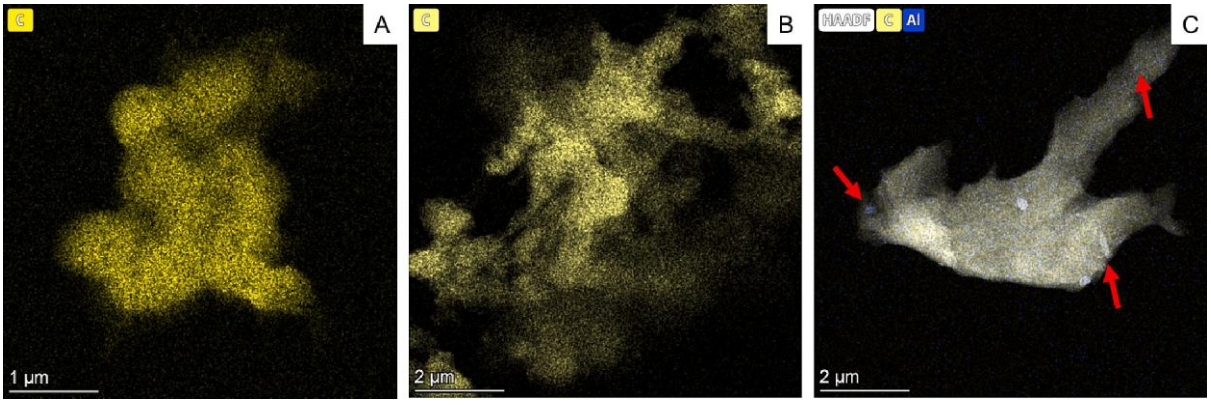


**Fig. 9.** TEM images of representative areas of (A) *E. coli* biofilm; (B) *E. coli* biofilm in the presence of PDA coating; (C) *E. coli* biofilm in the presence of PDA-HNTs/ **2** coating.

## 4. Experimental section

### *4.1. Materials and methods*

Column chromatographies were performed with Fluka silica gel, pore size 60 Å, 70–230 mesh, 63–200 µm. $^{1}$H NMR, $^{13}$C NMR and $^{19}$F NMR spectra were recorded at room temperature in $CD_3OD$ solution with an Agilent 500 spectrometer (Agilent Technologies, Santa Clara, CA, USA), operating at a frequency of 500 MHz for $^{1}$H, 125 MHz for $^{13}$C and 470 MHz for $^{19}$F using the residual solvent peak as internal refer-ence. For $^{19}$F NMR spectra, a small amount of $CFCl_3$ was added for the standard reference; chemical shifts ($\delta$) values are given in parts per million (ppm) and coupling constants ($J$) in Hertz. Melting points (un-corrected) were determined with a Kohfler melting points apparatus. For GC–MS analyses, the GC instrument GC-TRACE-ULTRA (THERMO electron corporation, Waltham, MA, USA) was equipped with a Fused silica capillary column OPTIMA-1–0.25 µm (30 m × 0.25 mm I.D.). Mass spectra were acquired with a POLARIS Q (THERMO electron corporation, Waltham, MA, USA) in EI mode (70 eV).

FT-IR spectra (KBr) were acquired with an Agilent Technologies Cary 630 FT-IR spectrometer (Agilent Technologies, Santa Clara, CA, USA).

The size analysis, ς-potential and polydispersity index of the samples were determined using a Malvern Zetasizer Nano ZS instrument (Mal-vern Instruments, Malvern, UK), fitted with a 532 nm laser at a fixed scattering

angle of 173°.

Thermogravimetric analyses (TGA) were performed on a Mettler Toledo instrument (Mettler Toledo, Barcelona, Spain), equipped with sensor and FRS5 microbalance (precision 0.1 μg) and FP89 software package, using a heating rate of 10 °C/ min in the 30–800 °C temper-ature range.

Transmission electron microscopy (TEM) was performed by means of a FEI Titan G2 60–300 ultra-high-resolution transmission electron mi-croscope (FEI, Lausanne, Switzerland) coupled with analytical electron microscopy (AEM) performed with a SUPER X silicon drift windowless energy dispersive X-ray spectroscopy (XEDS) detector. AEM spectra were saved in mode STEM (scanning transmission electron microscopy) with a HAADF (high angle annular dark field) detector.

$^{19}F$ and $^{27}Al$ solid state NMR were obtained at room temperature through a Bruker Avance II 400 MHz (9.4 T) spectrometer (Bruker, Billerica, MA, USA).

Contact angle measurements were performed by using an optical contact angle apparatus (OCA 20, Data Physics Instruments) equipped with a video measuring system having a high-resolution CCD camera and a high-performance digitizing adapter. SCA 20 software (Data Physics Instruments) was used for data acquisition. To obtain a tablet, the powder like material was pressed under 104 $kg \cdot cm^{-2}$ for 10 min. The contact angle of water in air was measured by the sessile drop method. The water droplet volume was 10.0 ± 0.5 mL. Temperature was set at 25.0 ± 0.1 °C for the support and the injecting syringe as well. Images were collected 25 times per second. From the data analysis the contact angle, the volume and the contact area of the drop were calculated. The volume of the droplet was constant within the time of the experiment.

All the chemicals were purchased from commercial sources and used as received without purification. Halloysite nanotubes used in this study were obtained from Merck (Darmstadt, Germany) and used as received.

### 4.2. *Spectrophotometric measurements*

Different aliquots of an aqueous dispersions of HNTs/**2** and HNTs/**5** nanomaterials were added to a 1 mL water solution of pyrene ($2 \times 10^{-7}$ M) in a final volume of 10 mL in $H_2O$. The obtained dispersions were degassed under air flow for 5 min. Steady-state fluorescence spectra were acquired with a JASCO FP-777 W spectrofluorimeter (Jasco Inc., Easton, MD, USA). Excitation, emission slits, excitation wavelength and emission interval are 1.5 nm, 1.5 nm, 337 nm and 340 – 450 nm, respectively.

### 4.3. *Synthesis of N-perfluoroacyl dopamides*

#### 4.3.1. *General procedure*

In a 100 mL round-bottom flask, while $N_2$ flux was maintained, degassed MeOH (30 mL) was introduced and $N_2$ was bubbled within the solution to remove dissolved $O_2$. Dopamine hydrochloride (1 eq) (ThermoFisher Scientific, 99%) was dissolved and then triethylamine (4.1 eq) (Merck, 99.5 %) and the

perfluoroacyl methyl ester (2 eq) were added to the flask. The resulting mixture was stirred at room temperature for 24 h. For perfluoroacyl methyl diesters, the amount of trie-thylamine and dopamine hydrochloride was doubled to 8.2 eq and 2 eq, respectively. After completion, the suspension was dried under reduced pressure. The crude product was dissolved in aqueous $NH_4Cl$ (100 mL, pH 5) and then extracted in ethyl acetate (3 × 50 mL). The organic phases were back-extracted with distilled water (3 × 30 mL), dried over $Na_2SO_4$, filtered and evaporated at reduced pressure. The crude product was dissolved in a minimum ethyl acetate volume and percolated through a silica column (eluent: ethyl acetate/hexane 7:3). The pure products were obtained as greyish and brownish solids.

*4.3.1.1. Synthesis of N-(3,4-dihydroxyphenethyl)-2,2,2-trifluoroacetamide (1).* Following the general procedure, dopamine hydrochloride (2.10 g, 11.2 mmol), triethylamine (4.65 g, 46.0 mmol), and methyl 2,2,2-trifluoroacetate (2.94 g, 23 mmol) (Fluorochem Limited UK, 99%) were mixed in 30 mL of MeOH. The mixture was stirred for 24 h. Yield 94%. 23 mmol) (Fluorochem Limited UK, 95%) were mixed in 50 mL of MeOH. The mixture was stirred for 24 h. Yield 93%.

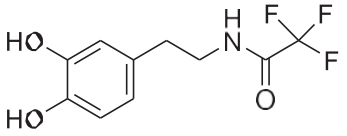


Pale brown powder. M.p. = 100–105 °C (lit. 103 °C).

$^1$H NMR (500 MHz, $CD_3OD$, 25 °C): $\delta$ = 6.69 (1H, d, 8.0 Hz); 6.65 (1H, d, 2.0 Hz); 6.52 (1H, dd, 8.0 Hz, 2.1 Hz); 3.42 (2H, t, 7.5 Hz); 2.72 (2H, m).

$^{19}$F NMR (470 MHz, $CD_3OD$, $CFCl_3$, 25 °C): δ = -75.77 (1F, s).

$^{13}$C NMR (125 MHz, $CD_3OD$, 25 °C): $\delta$ = 159.04 (q, $J_{C-F}$ 36.7 Hz); 146.36; 144.98; 131.40; 121.22; 117.59 (q, $J_{C-F}$ = 286.6 Hz); 116.98; 116.56; 42.68; 35.31.

*4.3.1.2. Synthesis of N-(3,4-dihydroxyphenethyl)-2,2,3,3,4,4,5,5,6,6,7,7,8,8,8-pentadecafluorooctanamide (2).* Following the general proced-ure, dopamine hydrochloride (2.2 g, 11.7 mmol), triethylamine (1.18 g, 26.91 mmol), and methyl 2,2,3,3,4,4,5,5,6,6,7,7,8,8,8-pentadecafluor-ooctanoate (5.00 g, 11.7 mmol) (Fluorochem Limited UK, 94%) were mixed in 50 mL of MeOH. The mixture was stirred for 24 h. Yield 92%.

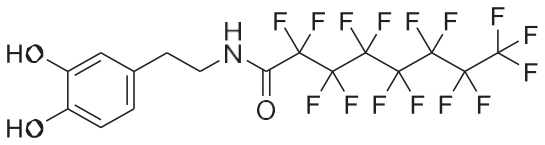

Pale brown powder. M.p. = 120–125 °C.

$^{1}$H NMR (500 MHz, $CD_3OD$, 25 °C): $\delta$ = 6.68 (1H, d, 8.0 Hz); 6.65 (1H, d, 2.0 Hz); 6.52 (1H, dd, 8.0 Hz, 2.1 Hz); 3.42 (2H, t, 7.5 Hz); 2.73 (2H, m).

$^{19}$F NMR (470 MHz, $CD_3OD$, $CFCl_3$, 25 °C): δ = -80.73 (3F, m); -119.13 (2F, t, 13.0 Hz); -120.79 (2F, m); -121.38 (2F, m); -121.93 (4F, m); -125.53 (2F, m).

$^{13}$C NMR (125 MHz, $CD_3OD$, 25 °C): $\delta$ = 159.35 (t, $J_{C-F}$ 27.0 Hz); 146.48; 145.10; 131.36; 121.24; 116.99; 116.54; 119.77 – 108.39 (CFx carbons); 43.03; 35.46.

*4.3.1.3. Synthesis of N-(3,4-dihydroxyphenethyl)-2,2,3,3,4,4,5,5,6,6,7,7,8,8,9,9,10,10,10-nonadecafluorodecanamide (3).* Following the gen-eral procedure, dopamine hydrochloride (2.10 g, 11.2 mmol), triethyl-amine (4.65 g, 46.0 mmol), and methyl 2,2,3,3,4,4,5,5,6,6,7,7,8,8,9,9, 10,10,10-nonadecafluorodecanoate (9.85 g, 23 mmol) (Fluorochem Limited UK, 97%) were mixed in 50 mL of MeOH. The mixture was stirred for 24 h. Yield 94%.

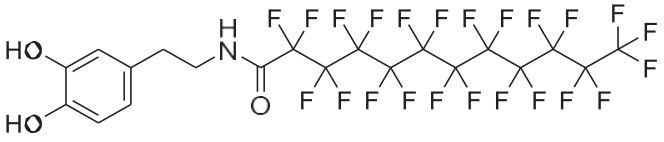

Pale brown powder. M.p. = 148–150 °C.

$^{1}$H NMR (500 MHz, $CD_3OD$, 25 °C): $\delta$ = 6.68 (1H, d, 8.0 Hz); 6.65 (1H, d, 2.0 Hz); 6.52 (1H, dd, 8.0 Hz, 2.0 Hz); 3.45 (2H, t, 7.6 Hz); 2.71 (2H, m).

$^{19}$F NMR (470 MHz, $CD_3OD$, $CFCl_3$, 25 °C): δ = -80.69 (3F, t, 10.1 Hz); -119.13 (2F, t, 12.5 Hz); -120.75--121.42 (8F, m); -122.06 (4F, m); -125.65 (2F, m).

$^{13}$C NMR (125 MHz, $CD_3OD$, 25 °C): $\delta$ = 159.37 (t, $J_{C-F}$ 25.8 Hz); 146.51; 145.13; 131.38; 121.25; 117.01; 116.57; 120.04 – 108.50 (CFx carbons); 43.05; 35.49.

*4.3.1.3.4.* Synthesis of N-(3,4-dihydroxyphenethyl)-2,2,3,3,4,4,5,5,6,6, 7,7,8,8,9,9,10,10,11,11,12,12,12-*tricosafluorododecanamide (4). Follo wing the general procedure, dopamine hydrochloride (2.10 g, 11.2 mmol), triethylamine (4.65 g, 46.0 mmol), and methyl 2,2,3,3,4,4,5,5,6, 6,7,7,8,8,9,9,10,10,11,11,12,12,12-tricosafluorododecanoate (9.85 g, 23 mmol) (Fluorochem Limited UK, 95%) were mixed in 50 mL of MeOH.*

*The mixture was stirred for 24 h. Yield 93%.*

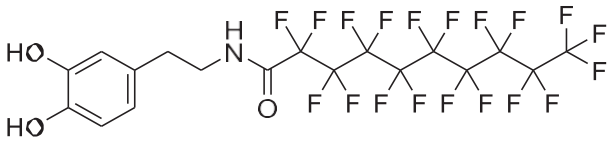

Pale brown powder. M.p. = 165–170 °C.

$^{1}$H NMR (500 MHz, $CD_3OD$, 25 °C): $\delta$ = 6.68 (1H, d, 8.0 Hz); 6.65 (1H, d, 2.0 Hz); 6.51 (1H, dd, 8.0 Hz, 2.0 Hz); 3.42 (2H, m); 2.73 (2H, m).

$^{19}$F NMR (470 MHz, $CD_3OD$, $CFCl_3$, 25 °C): δ = -80.72 (3F, t, 10.0 Hz); -119.19 (2F, t, 11.9 Hz); -120.81 - -121.47 (12F, m); -121.90 (4F, m); -125.59 (2F, m).

$^{13}$C NMR (125 MHz, $CD_3OD$, 25 °C): $\delta$ = 159.35 (t, $J_{C-F}$ 25.6 Hz);
146.49; 145.11; 131.37; 121.23; 116.99; 116.54; 119.75 – 110.00 (CFx carbons); 43.05; 35.49.

*4.3.1.3.5. Synthesis of N-(3,4-dihydroxyphenethyl)-2,2,3,3,4,4,5,5,6,6,7,7, 8,8,9,9,10,10,11,11,12,12,13,13,14,14,15,15,16,16,16-hentriaconta- fluorohexadecanamide (5).* Following the general procedure, dopamine hydrochloride (2.10 g, 11.2 mmol), triethylamine (4.65 g, 46.0 mmol), and methyl 2,2,3,3,4,4,5,5,6,6,7,7,8,8,9,9,10,10,11,11,12,12,13,13,1 4,14,15,15,16,16,16-hentriacontafluorohexadecanoate (9.85 g, 23 mmol) (Fluorochem Limited UK, 95%) were mixed in 50 mL of MeOH. To increase the solubility, 5 mL of DMF were also added. The mixture was stirred for 24 h. Yield 26%.

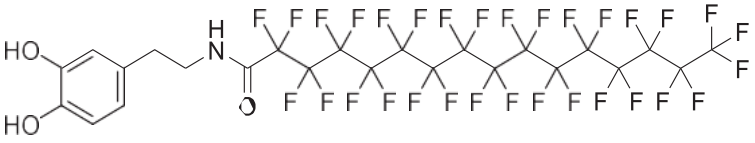

$^{1}$H NMR (500 MHz, DMSO-$d_6$), δ (ppm): 6.68 (1H, d, 8.0 Hz); 6.65
(1H, d, 2.0 Hz); 6.52 (1H, dd, 8.0 Hz, 2.1 Hz); 3.42 (2H, m); 2.73 (2H, m).

$^{19}$F NMR (470 MHz, DMSO-$d_6$, $CFCl_3$), δ (ppm): -79.73 (3F, t, 9.0 Hz); -114.35 (2F, t, 11.9 Hz); -120.70–121.42 (22F, m); -121.95 (2F, m); -121.93 (4H, m); -125.25 (2F, m).

$^{13}$C NMR (125 MHz, DMSO-$d_6$), δ (ppm): 159.39 (t, $J_{C-F}$ 25.9 Hz);
146.45; 145.06; 131.35; 121.23; 116.98; 116.53; 119.75 – 108.31 ($CF_x$ carbons); 43.03; 35.46.

*4.3.1.3.6. Synthesis of $N^1$,$N^6$-bis(3,4-dihydroxyphenethyl)-2,2,3,3,4,4,5,5-octafluorohexanediamide (6).* Following the general procedure, dopa-mine hydrochloride (0.87 g, 4.6 mmol), triethylamine (1.91 g, 19.0

mmol), and dimethyl 2,2,3,3,4,4,5,5-octafluorohexanedioate (0.73 g, 2.3 mmol) (Fluorochem Limited UK, 98%) were mixed in 50 mL of MeOH. The mixture was stirred for 24 h. Yield 91%.

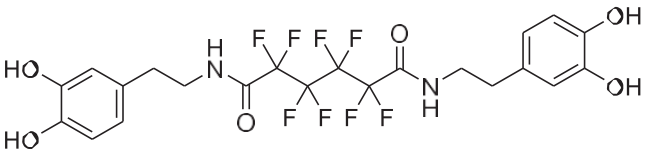

$^{1}$H NMR (500 MHz, $CD_3OD$, 25 °C): $\delta$ = 6.70 (1H, d, 8.0 Hz); 6.67 (1H, d, 1.9 Hz); 6.52 (1H, dd, 8.1 Hz, 1.9 Hz); 3.44 (2H, t, 7.5 Hz); 2.68 (2H, t, 7.5 Hz).

$^{19}$F NMR (470 MHz, $CD_3OD$, $CFCl_3$, 25 °C): δ = -121.10 (2F, m); -123.44 - -123.66 - -123.81 (2F,m).

$^{13}$C NMR (125 MHz, $CD_3OD$, 25 °C): $\delta$ = 159.77 (t, $J_{C-F}$ 26.3 Hz); 146.28; 144.89; 131.39; 121.24; 116.95; 116.53; 114.22–108.54 ($CF_x$ carbons); 42.93; 35.36.

### *4.4. Synthesis of the HNTs/1–6 nanomaterials*

To a dispersion of pristine HNTs in water (5 mL), 1 mL of a solution $1 \cdot 10^{-2}$ M of the corresponding molecule in MeOH was added. The ob-tained dispersion was sonicated (5 min, ultrasound power of 200 W, 25 °C), evacuated for 3 cycles and finally it was left under stirring for 18 h at room temperature. After this time, the dispersion was centrifuged and the obtained powder was washed with water, until the unreacted molecules were removed and, then dried at 60 °C overnight.

### *4.5. General procedure for PDA-HNTs/2 coating preparation*

Dopamine hydrochloride (40 mg, 10.6 mM) and HNTs/**2** (20 wt%) were dispersed in sodium acetate buffer at 50 mM (pH = 5.0) and the mixture was taken under vigorous stirring. Afterwards, sodium periodate was added to the reaction mixture to a final concentration of 10 mM, at a catechol/oxidant molar ratio of 1:1. Glass substrates (soaked in a piranha solution overnight) were dipped into the reaction mixture and left under stirring for 24 h, then rinsed with distilled water in an ul-trasonic bath, dried and analyzed by UV–*vis* spectrophotometry using a V-730 Jasco instrument (Fig. S4.). In control experiments the PDA deposition was run in the absence of modified HNTs nanomaterials.

### *4.6. Antimicrobial activity*

The Gram-negative *Escherichia coli* K12 DH10B (Invitrogen) was used as tester strains and were grown overnight in 3 mL Tryptic Soy Broth (TSB) broth at 37 °C and 30 °C, respectively, with constant orbital shaking at 180 rpm. Different suspensions of 1 mL of TSB containing each tester strain at the final concentration of $10^6$ CFU $mL^{-1}$ were incubated in sterile flat-bottom 24-well plates with different concentrations of compounds **1**–**6** (20, 100 and 500 μM) or HNTs based nanomaterials (final concentration of

organic molecules in HNTs of 20 μM). Pristine HNTs was also used at the maximum amount of 5 mg $mL^{-1}$. Plates were incubated for 24 h at 180 rpm at 37 °C. Parallel untreated cultivations and DMSO-treated cultivations were used as control growth conditions. Each cultivation was performed in triplicate. Bacterial growth was quantified by measuring the optical density at 600 nm using a microplate reader. ANOVA test was performed to infer statistical sig-nificance ($p < 0.05$).

### 4.7. *Inhibition of biofilm formation*

Inhibition of biofilm formation was investigated using a crystal violet (CV) assay as described in Raimondi *et al.,* 2019 with minor modification [50]. *E. coli* DH10B was incubated in test tubes with Tryptic Soy Broth (TSB) (5 mL) containing 2% w/v glucose at 37 °C and 30 °C respectively for 24 h at 180 rpm. In each well of a single cell culture polystyrene sterile, flat-bottom 24-well plate was added 25 μL of bacteria suspension and TSB with 2% w/v glucose (2 mL). Compounds **2**–**6** (final concen-tration of 20 μM) or HNTs based nanomaterials (final concentration of organic molecules in HNTs of 20 μM) were used to assess inhibition of biofilm formation. Parallel untreated cultivations and/or DMSO-treated cultivations were used as control conditions. Plates were incubated at 37 °C for 24 h statically. Then, the content of each well was removed, and wells were washed twice with 0.9% sterile NaCl and stained with 2 mL of 0.1% crystal violet solution for 30 min at room temperature. The excess solution was removed, and the plate was washed twice using tap water. A volume of 2 mL of ethanol was added to each stained well to solubilize the dye. Optical density (OD) was read with a wavelength of 590 nm using a microplate reader. All tests involved three biological replicates. The percentage of inhibition was calculated through the formula:

$$\%_{inhibition} = \left( \frac{OD_{growthcontrol} - OD_{sample}}{OD_{growthcontrol}} \right) \times 100 \qquad (1)$$

ANOVA test was performed to infer statistical significance ($p < 0.05$).

The bacterial biofilm for TEM analyses were prepared as above described with the addition of coverslips or PDA coating or PDA-HNTs/**2** nanocomposite coating (ca. 10 × 10 $mm^2$) in each well. After incubation at 37 °C for 24 h statically, the medium was discarded, and the cover-slips or the coatings were washed three times with sterile Phosphate-buffered saline (PBS) 1×, one time with sterile water and dried at 37 °C [49].

***CRediT authorship contribution statement:*** **Marina Massaro:** Methodology, Investigation, Writing – original draft, Writing – review & editing. **Maria Laura Alfieri:** Methodology, Investigation, Writing – original draft, Writing – review & editing. **Giorgio Rizzo:** Methodology, Writing – original draft. **Francesco Babudri:** Methodology, Investigation. **Teresa Faddetta:** Methodology, Investigation, Writing – original draft. **Giuseppe Gallo:** Methodology, Investigation, Writing – original draft. **Alessandra**

**Napolitano:** Meth-odology, Writing – original draft. **Rita Sanche`z-Espejo:** Methodology, Investigation. **Ce´sar Viseras Iborra:** Methodology, Writing – original draft. **Serena Riela:** Conceptualization, Supervision, Methodology, Writing – original draft, Writing – review & editing.

**Declaration of Competing Interest:** The authors declare that they have no known competing financial interests or personal relationships that could have appeared to influence the work reported in this paper.

**Data availability:** No data was used for the research described in the article.

**Acknowledgements:** The work was financially supported by the University of Palermo and University of Bari "A. Moro". This work was carried out in the fram of the PRIN2017-2017YJMPZN project. The ATeN Center (Med-CHHAB, PONa3 00273, University of Palermo) is acknowledged for technical support and laboratory hospitality. The authors thank Prof. G. Lazzara and Dr. G. Cavallaro (University of Palermo) for angle contact measurements.

**Appendix A. Supplementary data:** Supplementary data to this article can be found online.

## References

[1] B. Fazeli-Nasab, R.Z. Sayyed, L.S. Mojahed, A.F. Rahmani, M. Ghafari, S. Antonius, Sukamto, Biofilm production: a strategic mechanism for survival of microbes under stress conditions, Biocatal. Agri. Biotechnol. 42 (2022), 102337.

[2] H. Dang, C.R. Lovell, Microbial surface colonization and biofilm development in marine environments, Microbiol. Mol. Biol. Rev. 80 (1) (2016) 91–138.

[3] M. Assefa, A. Amare, Biofilm-associated multi-drug resistance in hospital-acquired infections: a review, Infect. Drug Resistance 15 (2022) 5061–5068.

[4] M. C´amara, W. Green, C.E. MacPhee, P.D. Rakowska, R. Raval, M.C. Richardson,

[5] J. Slater-Jefferies, K. Steventon, J.S. Webb, Economic significance of biofilms: a multidisciplinary and cross-sectoral challenge, npj Biofilms Microbiomes 8 (1) (2022) 42.

[6] G. Sharma, S. Sharma, P. Sharma, D. Chandola, S. Dang, S. Gupta, R. Gabrani, Escherichia coli biofilm: development and therapeutic strategies, J. Appl. Microbiol. 121 (2) (2016) 309–319.

[7] R. Roy, M. Tiwari, G. Donelli, V. Tiwari, Strategies for combating bacterial biofilms: a focus on anti-biofilm agents and their mechanisms of action, Virulence 9 (1) (2018) 522–554.

[8] X. Chen, S. Wu, D. Ma, J. Chen, Q. Guo, X. Han, K. Chen, H. Yang, Y. Huang, Y. Peng, A polyfluoroalkyl substituted phthalocyanine based supramolecular light switch for photothermal and photodynamic antibacterial activity against *Escherichia coli*, Chem. Commun. 54 (94) (2018) 13279–13282.

[9] V.V.T. Padil, K.P. Akshay Kumar, S. Murugesan, R. Torres-Mendieta, S. Wacławek, J.Y. Cheong, M. Cˇerník, R.S. Varma, Sustainable and safer nanoclay composites for multifaceted applications, Green Chemistry 24 (2022) 3081–3114.

[10] M.M. Abd El-Hady, A. Farouk, S. Sharaf, Multiwalled-carbon-nanotubes (MWCNTs)–GPTMS/tannic-acid-nanocomposite-coated cotton fabric for sustainable antibacterial properties and electrical conductivity, Coatings 12 (2) (2022) 178.

[11] A.T. Shah, S. Attique, M.A. ur Rehman, A.S. Khan, O. Goerke, 9 - Silica-based antibacterial coatings for dental implants, in: M.S. Zafar, Z. Khurshid, A.S. Khan, S. Najeeb, F. Sefat (Eds.), Dental Implants, Woodhead Publishing, 2020, pp. 145–171.

[12] L. Morillas-Becerill, L. De Cola, J.M. Zuidema, Inorganic nanoparticle empowered biomaterial hybrids: engineered payload release, Front. Nanotechnol. 4 (2022).

[13] M. Massaro, R. Ciani, G. Cin`a, C.G. Colletti, F. Leone, S. Riela, Antimicrobial nanomaterials based on halloysite clay mineral: research advances and outlook, Antibiotics 11 (12) (2022) 1761.

[14] L. Fan, W. Sun, Y. Zou, Q.-Q. Xu, R.-C. Zeng, J. Tian, Enhanced corrosion resistance, antibacterial activity and biocompatibility of gentamicin-montmorillonite coating on Mg alloy-in vitro and in vivo studies, J. Mater. Sci. Technol. 111 (2022) 167–180.

[15] K. Cherednichenko, D. Kopitsyn, S. Batasheva, R. Fakhrullin, Probing antimicrobial

[16] halloysite/biopolymer composites with electron microscopy: advantages and limitations, Polymers 13 (20) (2021) 3510.

[17] W. Wei, E. Abdullayev, A. Hollister, D. Mills, Y.M. Lvov, Clay nanotube/poly (methyl methacrylate) bone cement composites with sustained antibiotic release, Macromol. Mater. Eng. 297 (7) (2012) 645–653.

[18] S. Riela, M. Massaro, F. Parisi, G. Maniaci, F. Di Blasi, G. Spinelli, G. Biddeci, A. Baldizzi, G. Lazzara, METODO PER LA PREPARAZIONE DI NANOCOMPOSITI ANTIBATTERICI, 2019.

[19] Y. Li, X. Yuan, L. Jiang, H. Dai, Y. Zhao, X. Guan, J. Bai, H. Wang, Manipulation of the halloysite clay nanotube lumen for environmental remediation: a review, Environ. Sci. Nano 9 (3) (2022) 841–866.

[20] A. Stavitskaya, M. Rubtsova, A. Glotov, V. Vinokurov, A. Vutolkina, R. Fakhrullin, Y. Lvov, Architectural design of core–shell nanotube systems based on aluminosilicate clay, Nanoscale Adv. 4 (13) (2022) 2823–2835.

[21] D. Peixoto, I. Pereira, M. Pereira-Silva, F. Veiga, M.R. Hamblin, Y. Lvov, M. Liu, A. C. Paiva-Santos, Emerging role of nanoclays in cancer research, diagnosis, and therapy, Coord. Chem. Rev. 440 (2021), 213956.

[22] M. Massaro, G. Lazzara, R. Noto, S. Riela, Halloysite nanotubes: a green resource for materials and life sciences, Rendiconti Lincei 31 (2) (2020) 213–221.

[23] M. Massaro, A. Borrego-Sa´nchez, R. S´anchez-Espejo, C. Viseras Iborra, G. Cavallaro, F.

García-Vill´en, S. Guernelli, G. Lazzara, D. Miele, C.I. Sainz-Díaz, G. Sandri, S. Riela, Ciprofloxacin carrier systems based on hectorite/halloysite hybrid hydrogels for potential wound healing applications, Appl. Clay Sci. 215 (2021) 106310.

[24] A. Stavitskaya, C. Shakhbazova, Y. Cherednichenko, L. Nigamatzyanova, G. Fakhrullina, N. Khaertdinov, G. Kuralbayeva, A. Filimonova, V. Vinokurov, R. Fakhrullin, Antibacterial properties and in vivo studies of tannic acid-stabilized silver–halloysite nanomaterials, Clay Miner. 55 (2) (2020) 112–119.

[25] C. Tan, P. Zhao, Y. Zhou, M. Liu, Hydrophobic halloysite nanotubes via ball milling for stable pickering emulsions: implications for food preservation, ACS Appl. Nano Mater. 5 (8) (2022) 11289–11301.

[26] S. Majumder, C. Viau, A. Brar, J. Xia, S. George, Silver nanoparticles grafted onto tannic acid-modified halloysite clay eliminated multidrug-resistant *Salmonella typhimurium* in a Caenorhabditis elegans model of intestinal infection, Appl. Clay Sci. 228 (2022), 106569.

[27] O. Prinz Setter, I. Snoyman, G. Shalash, E. Segal, Gold Nanorod-incorporated halloysite nanotubes functionalized with antibody for superior antibacterial photothermal treatment, Pharmaceutics 14(10) (2022) 2094.

[28] W.O. Yah, A. Takahara, Y.M. Lvov, Selective modification of halloysite lumen with octadecylphosphonic acid: new inorganic tubular micelle, J. Am. Chem. Soc. 134

[29] (3) (2012) 1853–1859.

[30] H. Zhang, T. Ren, Y. Ji, L. Han, Y. Wu, H. Song, L. Bai, X. Ba, Selective modification of halloysite nanotubes with 1-pyrenylboronic acid: a novel fluorescence probe with highly selective and sensitive response to hyperoxide, ACS Appl. Mater. Interfaces 7 (42) (2015) 23805–23811.

[31] W.O. Yah, H. Xu, H. Soejima, W. Ma, Y. Lvov, A. Takahara, Biomimetic dopamine

[32] derivative for selective polymer modification of halloysite nanotube lumen, J. Am. Chem. Soc. 134 (29) (2012) 12134–12137.

[33] Q. Borjihan, J. Yang, Q. Song, L. Gao, M. Xu, T. Gao, W. Liu, P. Li, Q. Li, A. Dong, Povidone-iodine-functionalized fluorinated copolymers with dual-functional antibacterial and antifouling activities, Biomater. Sci. 7 (8) (2019) 3334–3347.

[34] J.-H. Kim, S.K. Park, J.-W. Lee, B. Yoo, J.-K. Lee, Y.-H. Kim, Hydrophobic perfluoropolymer thin-film encapsulation for enhanced stability of inverted polymer solar cells, J. Korean Phys. Soc. 65 (9) (2014) 1448–1452.

[35] G. Wen, Z. Guo, W. Liu, Biomimetic polymeric superhydrophobic surfaces and nanostructures: from fabrication to applications, Nanoscale 9 (10) (2017)

[36] 3338–3366.

[37] J. Saiz-Poseu, J. Mancebo-Aracil, F. Nador, F. Busque´, D. Ruiz-Molina, The chemistry behind catechol-based adhesion, Angew. Chem. Int. Ed. 58 (3) (2019) 696–714.

[38] M.L. Alfieri, T. Weil, D.Y.W. Ng, V. Ball, Polydopamine at biological interfaces, Adv. Colloid Interface Sci. 305 (2022) 102689.

[39] Z. Liu, B.-H. Hu, P.B. Messersmith, Acetonide protection of dopamine for the synthesis of highly pure N-docosahexaenoyldopamine, Tetrahedron Lett. 51 (18) (2010) 2403–2405.

[40] M. Massaro, S. Pieraccini, S. Guernelli, M.L. Dindo, S. Francati, L.F. Liotta, G. C. Colletti, S. Masiero, S. Riela, Photostability assessment of natural pyrethrins using halloysite nanotube carrier system, Appl. Clay Sci. 230 (2022) 106719.

[41] M. Massaro, M. Casiello, L. D'Accolti, G. Lazzara, A. Nacci, G. Nicotra, R. Noto, Pettignano, C. Spinella, S. Riela, One-pot synthesis of ZnO nanoparticles supported on halloysite nanotubes for catalytic applications, Appl. Clay Sci. 189 (2020) 105527.

[42] S. Riela, A. Barattucci, D. Barreca, S. Campagna, G. Cavallaro, G. Lazzara, M. Massaro, G. Pizzolanti, T.M.G. Salerno, P. Bonaccorsi, F. Puntoriero, Boosting the properties of a fluorescent dye by encapsulation into halloysite nanotubes, Dyes Pigm. 187 (2021) 109094.

[43] K.J.D. MacKenzie, D.R.M. Brew, R.A. Fletcher, R. Vagana, Formation of aluminosilicate geopolymers from 1:1 layer-lattice minerals pre-treated by various methods: a comparative study, J. Mater. Sci. 42 (12) (2007) 4667–4674.

[44] J.T. Kloprogge, C.P. Ponce, Spectroscopic studies of synthetic and natural saponites: a review, Minerals 11 (2) (2021) 112.

[45] S. Das, S. Jana, A tubular nanoreactor directing the formation of in situ iron oxide nanorods with superior photocatalytic activity, Environ. Sci. Nano 4 (3) (2017) 596–603.

[46] M. Massaro, S. Riela, G. Cavallaro, C.G. Colletti, S. Milioto, R. Noto, G. Lazzara, Ecocompatible halloysite/cucurbit[8]uril hybrid as efficient nanosponge for pollutants removal, ChemistrySelect 1 (8) (2016) 1773–1779.

[47] O. Prinz Setter, E. Segal, Halloysite nanotubes – the nano-bio interface, Nanoscale 12 (46) (2020) 23444–23460.

[48] M. Kim, M.K. Shin, J.-S. Sung, A.A. Kadam, Supermagnetic halloysite nanotubes surface-tuned with aminosilane for protease immobilization and applied for eradication of bacterial biofilm, Appl. Surf. Sci. 593 (2022), 153469.

[49] C.S. Alves, M.N. Melo, H.G. Franquelim, R. Ferre, M. Planas, L. Feliu, E. Bardají, W. Kowalczyk, D. Andreu, N.C. Santos, M.X. Fernandes, M.A.R.B. Castanho, *Escherichia coli* cell surface perturbation and disruption induced by antimicrobial peptides BP100 and pepR*, J. Biol. Chem. 285 (36) (2010) 27536–27544.

[50] J.S. Dickson, M. Koohmaraie, Cell surface charge characteristics and their relationship to

bacterial attachment to meat surfaces, Appl. Environ. Microbiol. 55 (4) (1989) 832–836.

[51] L. Lisuzzo, G. Cavallaro, P. Pasbakhsh, S. Milioto, G. Lazzara, Why does vacuum drive to the loading of halloysite nanotubes? The key role of water confinement, J. Colloid Interface Sci. 547 (2019) 361–369.

[52] M. Massaro, F. Armetta, G. Cavallaro, D.F. Chillura Martino, M. Gruttadauria, G. Lazzara, S. Riela, M. d'Ischia, Effect of halloysite nanotubes filler on polydopamine properties, J. Colloid Interface Sci. 555 (2019) 394–402.

[53] P.P. Mahamuni-Badiger, P.M. Patil, M.V. Badiger, P.R. Patel, B.S. Thorat- Gadgil, A. Pandit, R.A. Bohara, Biofilm formation to inhibition: Role of zinc oxide-based nanoparticles, Mater. Sci. Eng. C 108 (2020), 110319.

[54] S. Federico, V. Catania, F.S. Palumbo, C. Fiorica, D. Schillaci, G. Pitarresi, G. Giammona, Photothermal nanofibrillar membrane based on hyaluronic acid and graphene oxide to treat *Staphylococcus aureus* and *Pseudomonas aeruginosa* infected wounds, Int. J. Biol. Macromol. 214 (2022) 470–479.

[55] M.V. Raimondi, R. Listro, M.G. Cusimano, M. La Franca, T. Faddetta, G. Gallo, D. Schillaci, S. Collina, A. Leonchiks, G. Barone, Pyrrolomycins as antimicrobial agents. Microwave-assisted organic synthesis and insights into their antimicrobial mechanism of action, Bioorg. Med. Chem. 27 (5) (2019) 721–728.